LUMEN ET VIRTUS
ISSN: 2177-2789

IMPLEMENTATION OF VECTOR MODULATION APPLIED TO THE VSI THREE-PHASE DC-AC CONVERTER USING FOUR-STATE SWITCHING CELL

https://doi.org/10.56238/levv15n41-077

Submitted on: 09/22/2024 **Publication date:** 10/22/2024

Douglas Romeu Reif[1], Romeo Hausmann[2] and Sérgio Vidal Garcia Oliveira[3]

ABSTRACT

This paper presents the implementation of spatial vector modulation applied to the three-phase VSI converter with four-state switching cell. The methodology used is shown in detail, indicating the vectors used, the switching sequence applied and the calculations of the vector activation times. In addition, it contains the result of the operation of the converter in simulation, showing the main waveforms. Next, he brings the results obtained by experimentation with the assembled prototype.

Keywords: Switching cells. DC/AC converters. Multilevel inverters. Spatial vector modulation.

[1]Regional University of Blumenau, Blumenau – SC, Brazil
E-mail: douglasrreif@gmail.com
[2]Regional University of Blumenau, Blumenau – SC, Brazil
[3]Regional University of Blumenau, Blumenau – SC, Brazil

INTRODUCTION

Multilevel converters have been studied and implemented for more than three decades [1], several authors have developed topologies and new ways to control these converters. Among the most used topologies can be mentioned the one with a stapled diode [1]. Increasingly popular due to their high power processing capacity [2] and [3], these converters can be controlled by different methods, using sine pulse width modulation (SPWM), selective harmonic elimination (SHEPWM) and spatial vector modulation (SVM) [1] - [4]. For each technique there are different variations, depending on which objective to be employed. Some examples of variations: for common mode voltage reduction, operate with overmodulation index, decrease total harmonic distortion, decrease switching losses [1] - [4].

The topological structure presented in this paper was implemented by [5] and [6], who used the modulation technique (SPWM) obtaining satisfactory results in simulation and experimentation with a prototype. The big news in this article is the implementation of the modulation technique (SVM) to control the eighteen switches of the structure, hitherto unheard of for this converter application using four-state switching cells. In the article, the operation of the structure is first explained, followed by the theoretical part of the development of the modulation technique (SVM). To prove the operation of the modulation (SVM) the results are shown by simulation, and finally, these are compared with the results of the experiment using a prototype.

STRUCTURE AND VECTOR MODULATION

The structure of the topology presented in Figure 1. was developed by [5] and later implemented by [5] and [6], this structure not only reduces the voltage forces on the switches, but also reduces the current forces. This is due to the use of coupled three-phase inductors, which allow the phase current to be divided symmetrically between the converter arms.

Figure 1 DC-AC converter topology with four-state switching cell.

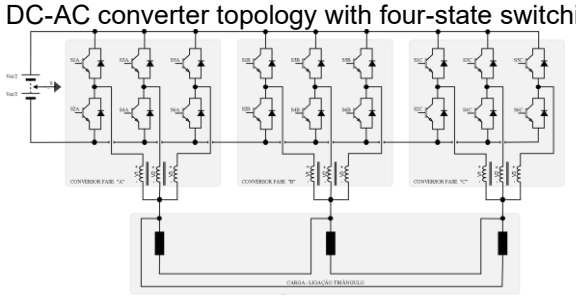

In this way the current circulating in the switches is 1/3 phase output. The frequency of the voltage waveform at the output of each phase is three times the switching frequency of the switches. This means that the volumes of the outlet filters are smaller. According to [5], with these characteristics the application of this converter is better for medium and high power applications.

OPERATING PRINCIPLE

The basic principles of operation of the structure are: each phase has three arms, the actuations of the upper switches of each arm are 180° out of step in relation to the lower ones. This means that whenever the upper switches are turned on, the lower ones must be turned off, to avoid an arm short circuit, the dead times must be entered according to the switching characteristics of the semiconductors. The arms are 120° out of step between them, this offset is extremely important for the correct operation of the converter, the balance of the current division of each arm intrinsically depends on this lag.

For the three-phase system to be implemented, between the phases there must also be a 120° lag in the low frequency. According to [5], the use of two switches per arm and with complementary control of each other, and the use of three arms in the four-state switching cell, generates a vector combination of 2^3. Eight switch combinations are possible. Evaluating for the three-phase structure there are 8^3 possible combinations, which means that 512 topological states are possible to execute.

SPATIAL VECTOR ANALYSIS

The effective switching of the structure apart from the redundant vectors is 4^3, i.e. 64 combinations. In Figure 2, the upper and lower switches are replaced by voltage sources. Such sources are the results of the output voltage of the three-phase coupled inductor, which depending on the selected vector will generate a different level of voltage, TABLE II shows this behavior in detail.

Figure 2 Rearranged structure with the four-state switching switches.

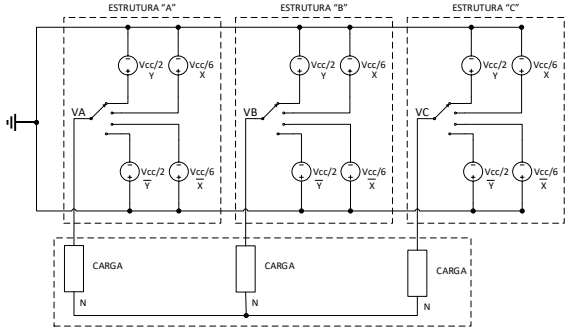

This methodology is used to map and organize the vectors, so the vectors will be separated into groups of six. The resulting vector of each group is obtained graphically using vector geometry. The full vector map is shown in Figure 3.

Figure 3 Complete vector map.

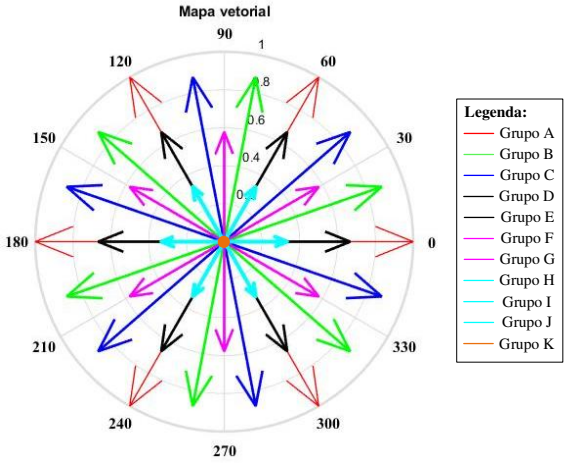

From the vector map in Figure 3, the envelopes of the resulting vectors are interconnected, thus forming thirty-six equilateral triangles. Figure 4 shows the hexagon formed by the connection of the points and the location of the sectors.

DEFINITION OF SWITCHING SECTORS AND CLASSES

According to [7], the reference vector shown in Figure 4 is the result of the transformation of the three-phase sinusoidal system into the axes (αβ) of the Clarke transform. In this way, the three-phase system can be simplified and the reference vector will be the result of the transform.

Figure 4 Hexagon with the location of sectors and classes.

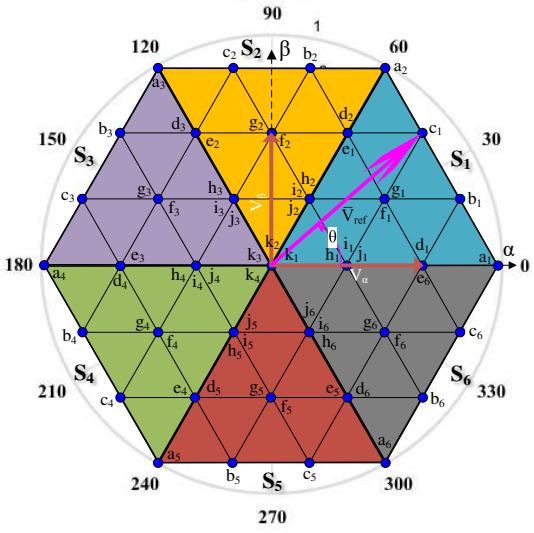

$$V_\alpha = \sqrt{\frac{2}{3}}\left(V_{ab} \quad \frac{-V_{bc}}{2} \quad \frac{-V_{ca}}{2}\right) \qquad (1)$$

where:

V_α - reference stress on the shaft (α);

V_{ab} - line voltage, measured between phases A and B;

V_{bc} - line voltage, measured between phases B and C;

V_{ca} - line voltage, measured between phases C and A.

$$V_\beta = \sqrt{\frac{2}{3}}\left(0 + \frac{\sqrt{3}}{2}V_{bc} \quad -\frac{\sqrt{3}}{2}V_{ca}\right) \qquad (2)$$

where:

V_β - reference voltage on the shaft ().β

$$\vec{\mathbf{V}}_{\mathbf{ref}} = \mathbf{V}_{\boldsymbol{\alpha}} + \mathbf{j}\mathbf{V}_{\boldsymbol{\beta}} \qquad (3)$$

where:

$\vec{V}_{ref}$- Reference vector.

$$\boldsymbol{\theta} = \mathbf{tan}^{-1}\left(\frac{\mathbf{V}_{\boldsymbol{\beta}}}{\mathbf{V}_{\boldsymbol{\alpha}}}\right) \qquad (4)$$

where:

$\boldsymbol{\theta}$- angle of the reference vector.

The previous equations do not show the exact location of the reference vector, it only shows in which sector it is located. To mark the exact position of the reference vector, it must be determined which class it belongs to. The switching class is made up of the three closest vectors. Figure 5 illustrates with an example the position of the reference vector within sector 1 and class VI.

Figure 5 Location of the reference vector.

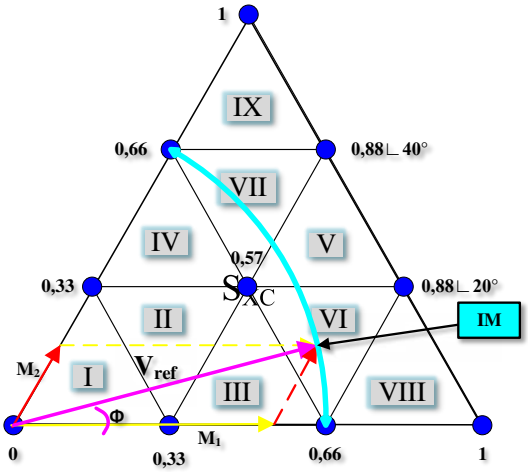

In order to lock the position of the reference vector, some constraints were implemented as shown in TABLE I. According to [7] the values of the generic constraint vectors are obtained by applying the expressions:$M_1 M_2$

$$\boldsymbol{M_1 = \frac{\sqrt{3}|V_{ref}|}{V_{cc}} sin(60 - \emptyset)} \qquad (5)$$

where:

M_1 - generic constraint vector referenced on the axis ();α

V_{cc} - direct current (DC) bus voltage;

$\emptyset$ - Constraint angle, for class location.

$$\boldsymbol{M_2 = \frac{\sqrt{3}|V_{ref}|}{V_{cc}} sin(\emptyset)} \qquad (6)$$

where:

M_2 - generic vector of constraint referenced on the axis ().α

TABLE I. Constraints of each class for implementation in the command algorithm

Class	Condition
I	$I_M < 0{,}285$
II	$\begin{cases} 0{,}286 < I_M < 0{,}569 \\ M_2 > 0{,}28 \end{cases}$
III	$\begin{cases} 0{,}33 < I_M < 0{,}569 \\ M_1 > 0{,}33 \\ \emptyset < 0{,}30 \end{cases}$
IV	$\begin{cases} 0{,}33 < I_M < 0{,}569 \\ M_2 > 0{,}33 \\ \emptyset > 0{,}30 \end{cases}$
V	$\begin{cases} 0{,}57 < I_M < 0{,}879 \\ 0{,}33 < M_1 < 0{,}815 \\ 0{,}33 < M_2 < 0{,}815 \\ 0{,}20 < \emptyset < 0{,}40 \end{cases}$

SAW	$\begin{cases} 0{,}57 < I_M < 0{,}879 \\ M_1 > 0{,}571 \\ \emptyset < 0{,}30 \end{cases}$
VII	$\begin{cases} 0{,}57 < I_M < 0{,}879 \\ M_2 < 0{,}571 \\ \emptyset > 0{,}30 \end{cases}$
VIII	$\begin{cases} 0{,}661 < I_M < 0{,}879 \\ M_1 > 0{,}662 \\ \emptyset < 0{,}20 \end{cases}$
IX	$\begin{cases} 0{,}661 < I_M < 0{,}879 \\ M_2 > 0{,}662 \\ \emptyset > 0{,}40 \end{cases}$

DEFINITION OF VECTOR APPLICATION TIMES

The reference vector to be synthesized is dependent on the time at which the three closest vectors are bound. From the calculus of $M_1$and ,M_2 applying the constraints we find the class of commutation, the nearest vectors are represented by , and . The average value of the reference vector can be expressed by equation (7).$\vec{V}_1\vec{V}_2\vec{V}_0$

$$\vec{V}_{ref} = \frac{1}{T_s}\left(\int_0^{t_1} \vec{V}_1\, dt + \int_{t_1}^{t_2} \vec{V}_2\, dt + \int_{t_2}^{t_0} \vec{V}_0\, dt\right) \qquad (7)$$

where:

$\vec{V}_1, \vec{V}_2, \vec{V}_0$ - nearest vectors used in the calculation of switching time,

t_1, t_2, t_0 - application time of the closest vectors;

T_s - switching period.

Equation (7) can be written as:

$$\vec{V}_{ref} = \frac{t_1}{T_s}\vec{V}_1 + \frac{t_2}{T_s}\vec{V}_2 + \frac{t_0}{T_s}\vec{V}_0 \qquad (8)$$

Decomposing the vectors of equation (8) to the axes of the plane (αβ) and separating the vector variables, we find equations (9) and (10).$\vec{V}_\alpha$ e $\vec{V}_\beta$

$$\vec{V}_\alpha = \frac{t_1}{T_s}\vec{V}_{1\alpha} + \frac{t_2}{T_s}\vec{V}_{2\alpha} + \frac{t_0}{T_s}\vec{V}_{0\alpha} \qquad (1)$$

$$\vec{V}_\beta = \frac{t_1}{T_s}\vec{V}_{1\beta} + \frac{t_2}{T_s}\vec{V}_{2\beta} + \frac{t_0}{T_s}\vec{V}_{0\beta} \qquad (2)$$

where:

$\vec{V}_{1\alpha}, \vec{V}_{2\alpha}, \vec{V}_{0\alpha}$ - vectors decomposed to the axis (α);

$\vec{V}_{1\beta}, \vec{V}_{2\beta}, \vec{V}_{0\beta}$ - vectors decomposed to the axis (β).

The sum of the times cannot be greater than the period of commutation. We have:

$$t_1 + t_2 + t_0 = T_s \qquad (11)$$

DEFINITION OF THE SWITCHING SEQUENCE

According to [8], the switching sequence should be the one that generates the lowest switching in semiconductors and allows the least harmonic distortion of the converter's output voltage. For the converter in question, the balance of the currents in the switches on the upper part of the arms must be observed. The switching sequence to be used will be to keep the currents balanced between the switches, a criterion that guarantees one of the main advantages of the structure and thus redundant vectors are eliminated.

To exemplify the choice of the switching sequence, the modulation index IM=0.9 is used, remembering that for this modulation index the vectors of classes VIII and IX remained active.

Following the operating sequence of the converter, it starts with sector 1, the switching sequence within a switching period is formed V6→V7→V3→V7→V5→V7 for classes VIII and IX. Table II shows which switches are activated for each chosen vector.

TABLE II. Relationship of vectors and switch command

Vectors	S1X	S3X	S5X	S2X	S4X	S6X	Tension
V8	0	0	0	1	1	1	-E/2
V1	0	0	1	1	1	0	-E/6
V2	0	1	0	1	0	1	-E/6
V4	1	0	0	0	1	1	-E/6
V3	0	1	1	1	0	0	E/6
V5	1	0	1	0	1	0	E/6
V6	1	1	0	0	0	1	E/6
V7	1	1	1	0	0	0	E/2

TABLE III presents the summary of the switching sequence for each sector and class at the modulation index at 0.9. For the three-phase system, the 120º lag between the phases is obtained by the lag of the operating sectors, Table IV shows the comparison of the position that each sector should be in relation to the other.

TABLE III. Summary of the switching sequence for phase A IM=0.9

Sector	Classes	Switching sequence	Voltage level
1	VIII	V6→V7→V3→V7→V5→V7	first
	IX	V6→V7→V3→V7→V5→V7	first
2	VIII	V6→V7→V3→V7→V5→V7	first
	IX	V2→V3→V1→V5→V4→V6	second
3	VIII	V2→V3→V1→V5→V4→V6	third
	IX	V8→V2→V8→V1→V8→V4	room
4	VIII	V8→V2→V8→V1→V8→V4	room
	IX	V8→V2→V8→V1→V8→V4	room
5	VIII	V8→V2→V8→V1→V8→V4	room
	IX	V2→V3→V1→V5→V4→V6	third
6	VIII	V2→V3→V1→V5→V4→V6	second
	IX	V6→V7→V3→V7→V5→V7	first

According to table IV, it is concluded that the switching sequence of the other phases are the same as in phase A, the difference will be in the sector that each phase is in. If phase A is in sector 1, the switching sequence used is V6→V7→V3→V7→V5→V7, in the same row of table IV phase B is in sector 3 and the switching sequence is V2→V3→V1→V5→V4→V6 and phase C is in sector 5 with the sequence V8→V2→V8→V1→V8→V4.

TABLE IV. Three-phase system sectors

Phase A	Phase B	Phase C
S1	S3	S5
S2	S4	S6
S3	S5	S1
S4	S6	S2
S5	S1	S3
S6	S2	S4

In this way, the three-phase converter output system is mounted and the line voltage is obtained by measuring the potential difference between the phases.

SIMULATION RESULTS

The simulation results of the three-phase voltage and current waveforms were obtained with the following converter parameters:

- DC bus voltage = 310V;
- switching frequency = 9kHZ;
- MI modulation index = 0.9;
- power strip inductors = 0.2mH;
- power strip capacitors = 10uF;
- three-phase output power = 9kW connected in triangle;
- single-phase output power = 3kW.

Waveforms of the line voltages before and after the filter, the currents of the coils of the coupled inductor, the phase currents before and after the filter are displayed. These waveforms are just a comparison with the waveforms of the prototype.

Figure 6 presents the waveform of the phase voltage for IM = 0.9, this voltage is obtained by measuring the output of the three-phase inductor coupled to the central connection point of the capacitors on the DC bus, by inspection it is possible to verify the indications of the voltage levels, highlighting the four levels of each phase, in accordance with TABLE III.

Figure 6 Phase voltage waveform, for IM = 0.9.

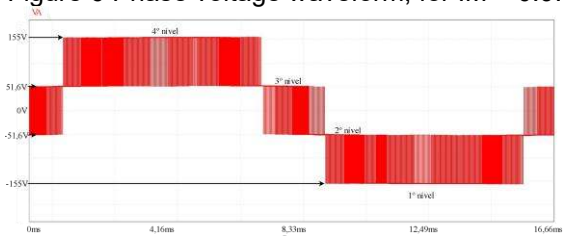

Figure 7 shows the VAB line voltage, measured between the phases at the output of the coupled three-phase inductor and its waveform is in accordance with what is expected compared to the theory. This statement is possible because of the indication of the levels. By inspection, the seven voltage levels are found.

Figure 7 Line voltage waveform, for IM = 0.9.

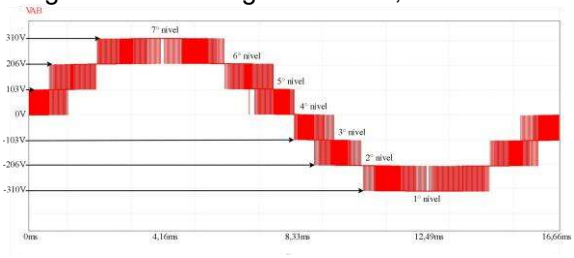

Figure 8 shows the line voltages after the output filter. The peak value is 229V and the effective value or RMS is 161V, this value can be calculated by applying the expression

$$V_{RMS} = \frac{Vcc \times I_M}{\sqrt{3}} = \frac{310 \times 0{,}9}{\sqrt{3}} = 161V \qquad (3)$$

where:

V_{RMS} - effective line voltage, measured at load;

Vcc - DC bus voltage;

I_M - modulation index.

Figure 8 Waveforms of line voltages after the power strip, with IM = 0.9.

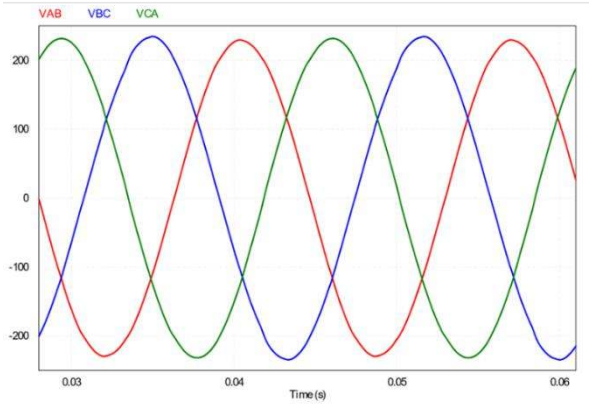

Evaluating Figure 9 is the graphs of the currents of each coil of the coupled inductor I(MUTA_1), I(MUTA_2) and I(MUTA_3) applied to phase A, as well as its output current (Ia). The peak value of the output current is close to 46.5A, this current is line. To have the phase value it is divided by √3, consequently the phase current is close to 26.8A peak.

Figure 9 Waveforms of the currents in the coils of the coupled inductor of phase A, with IM = 0.9.

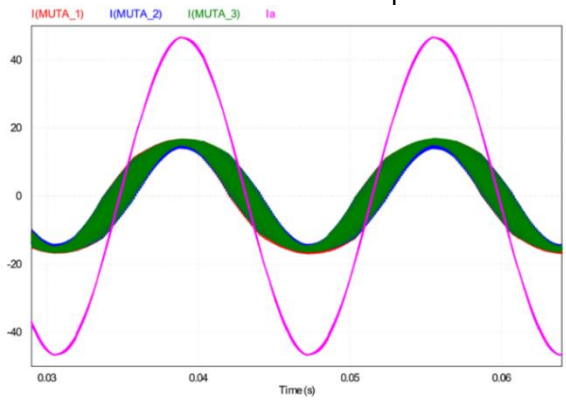

To exemplify the formation of the output current, in Figure 10, the instantaneous value of each of the inductor currents was scored for the time instant 0.0419615. The sum of the instantaneous currents forms the value of the output current. Based on the above, it is clear that each coil is responsible for conducting 1/3 of the output current, in addition to all currents are switching in the switching period. Figure 10 shows the waveforms of the currents in the coils of the phase A coupled inductor in a switching period.

Figure 10 Waveforms of currents in the coils of the phase A coupled inductor in detail, with IM = 0.9.

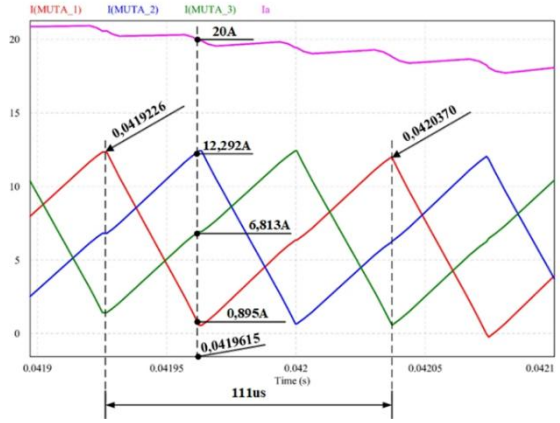

Figure 11 shows the shapes of the phase currents. It turns out that the peak current is approximately 26.5A, so the RMS current is 18.73A. The RMS current can be calculated by applying equation 13.

$$\mathrm{I_{RMS}} = \frac{\mathrm{P}}{\mathrm{V_{RMS}}} = \frac{3000}{161} = 18{,}63\mathrm{A} \qquad (4)$$

where:

I_{RMS} - effective current, measured at load;

P - single-phase active output power.

Figure 11 Waveforms of phase currents, measured at load, for IM = 0.9.

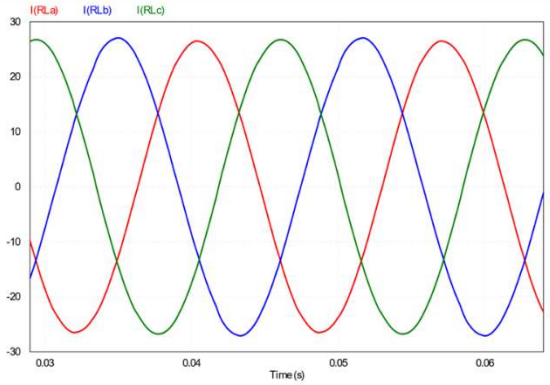

The output power waveform for phase A is shown in Figure 12. This power waveform is the result of the point-to-point multiplication of the line voltage (Vab) by the phase I current (RLa). The value that generates dissipated power is the average value of the power. Checking Figure 12 the peak output power is 6000W, so the average value is 3000W.

The results presented using the PSIM simulations will be used to validate the experimental results of the prototype.

Figure 12 Waveforms of phase currents, phase voltage, and power, for IM = 0.9.

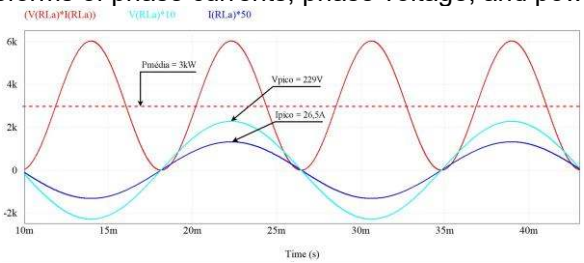

EXPERIMENTAL RESULTS

In this section, the results obtained in the prototype are presented. Figure 13 shows the equipment used in the experiment.

Figure 13 Image of the prototype.

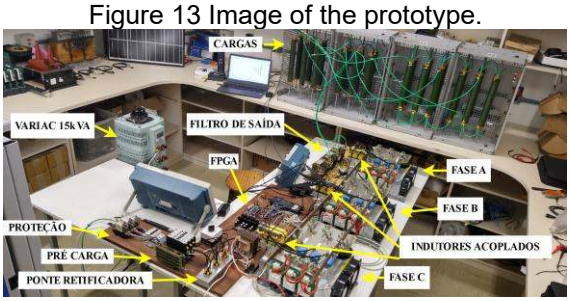

The experimental results are compared with the simulated results, all using the same modulation index of 0.9. Starting the analysis with the phase voltages, as shown in Figure 6, we see that the shape of the voltages has four well-defined levels, with positive and negative peaks at 1/2 Vdc and intermediate levels at 1/6 Vdc. Figure 14 shows the phase voltages with the DC bus at 310V. It is verified that there are four voltage levels, analyzing the scale used in the oscilloscope, there are peaks of 155V positive and negative and in the intermediate levels the voltages of approximately 51.66V.

Figure 14 Waveforms of phase voltages, measured before the power strip, at the output of the coupled inductor relative to the midpoint between the DC bus capacitors.

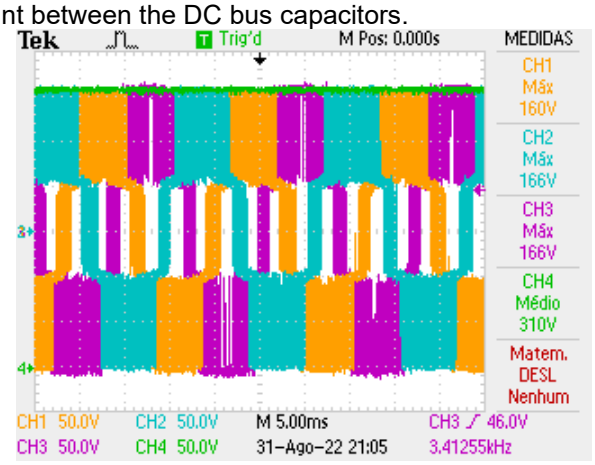

Similar to Figure 7, Figure 15 shows the line voltages before the output filter. Both waveforms have seven voltage levels, where each level can be found every 103V approximately. It is possible to observe that the voltages were obtained with the DC bus at 310V, as shown in CH1.

Figure 15 Waveform of the line voltages before the filter, Vab, Vbc, and Vca.

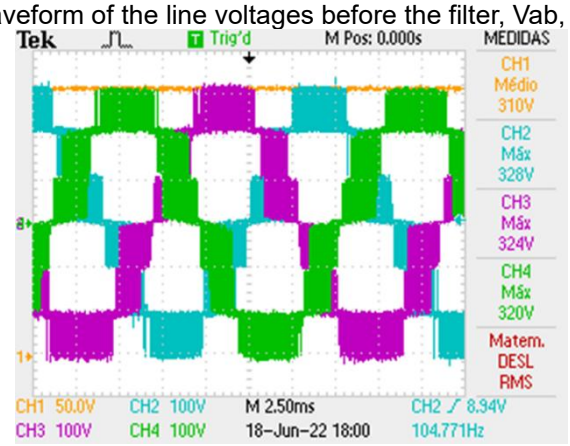

CH2 refers to the line voltage Vab, measured with the positive ferrule at the output of the phase A coupled inductor relative to the output of the phase B coupled inductor. The line voltage shown on channel CH3 refers to the measurement between the output of the phase B coupled inductor relative to the output of the phase C coupled inductor, and the line voltage of the CH4 channel is the measurement between the output of the coupled inductor of phase C in relation to the output of the coupled inductor of phase A.

In Figure 16 the waveforms of the voltages in the load are shown, again channel 1 represents the DC bus voltage at 310V. It is visible that both graphs have a sinusoidal shape, as an example the waveform of channel 2, it is observed that the frequency of the sine is approximately 60Hz, with an effective voltage value of 160V and a peak at 220V, same as shown in Figure 8.

Figure 16 Waveforms of voltages A, B and C measured at the load with IM=0.9 showing the sinusoidal format at the frequency of 60Hz, with RMS voltage of 160V.

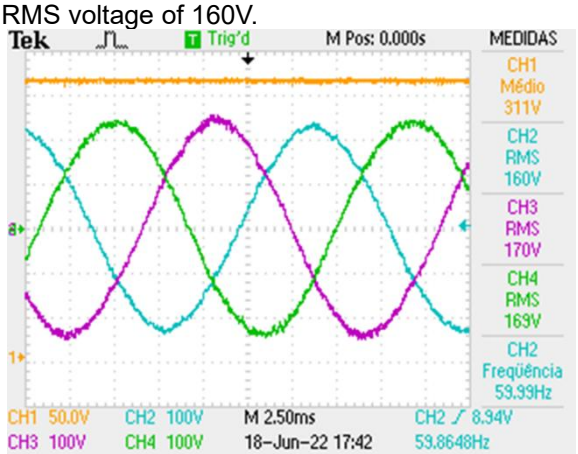

Analogous to Figure 9, Figure 17 shows the waveforms of the currents of the three-phase coupled inductor. It is possible to check the balance of the currents, this happens because the time applied to the vectors are divided in equal proportions.

Figure 17 Waveforms of the currents of the three-phase coupled inductor of phase A, in green the output voltage and red the same output current using the mathematical function of the oscilloscope, in this function the currents of channels 1, 2 and 3 were added.

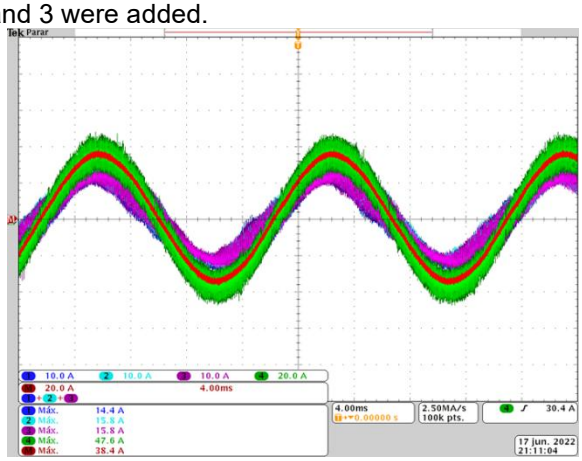

According to Figure 18 and comparing with Figure 10, there is an enlarged picture of the currents in the three-phase coupled inductor. The switching frequency is respected, both are at 9kHz, a parameter that was indicated at the beginning of the project. There is balance in the waveforms, both in Figure 18 and Figure 10 there is a proportion of 1/3 of the currents in relation to the output current of the coupled inductor, this effect reduces the current forces applied to the switches. The imbalance between the currents is caused by the physical mounting of the three-phase coupled inductor. Here an EE type core was used, the central leg of the core is double the lateral ones, in order to keep the inductance value symmetrical between the three coils, a manual adjustment is made to the *gap* of the central leg, until it reaches the calculated value. All this adjustment generates a small imbalance that does not influence the proper functioning of the converter.

Figure 18 High-frequency detail of the currents of the three-phase coupled inductor of phase A, showing the balance of the currents in the three coils and the sliders a and b, demonstrating that the switching frequency is 9kHz.

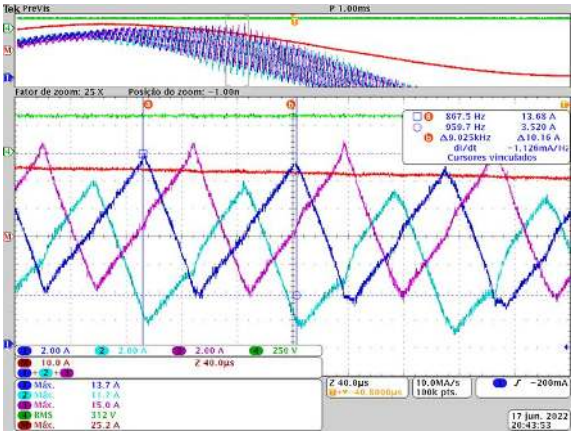

As shown in Figure 19, which shows the shapes of the currents in the load, it is emphasized that the DC bus voltage, shown in channel 4, is 310V. The frequencies of the currents are very close to 60Hz.

Figure 19 Waveforms of phase currents, measured with the current tips on the load, between the closures at the delta connection.

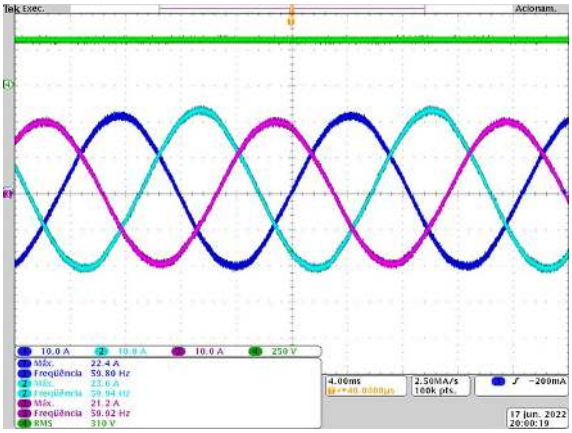

Figure 20 shows the final result, similar to what is done in Figure 12. Channel 1 measures the current at the load and channel 2 the voltage. The mathematical function of the oscilloscope was used to multiply the waveforms point by point, the result of this function was an average power of 3kW per phase. It can be stated that the power of 9kW three-phase was obtained.

Figure 20 Waveform of the output power, generated from the load current of phase A multiplied by the voltage of phase A.

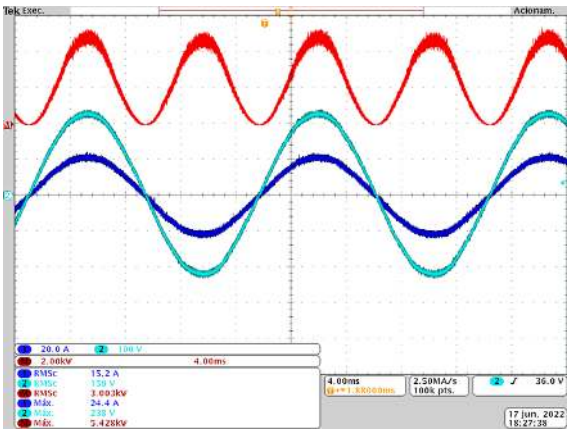

Even the harmonic voltage distortion, shown in Figure 21, indicates the proper functioning of the converter. In the figure, the distortions were compared between the simulation, using the PWM switching method, and also by simulation, the vector modulation and both in relation to the prototype.

Figure 21 Comparison of harmonic voltage distortion

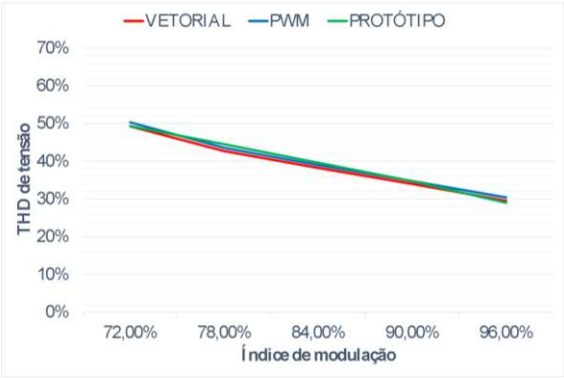

CONCLUSIONS

In this article, the spatial vector modulation technique applied to the three-phase DC-CA VSI converter was presented, using four-state switching cells, showing the applied vectors, vector switching sequence, as well as the vector application times. The theory developed was proven through computer simulation, using the PSIM software, bringing the waveforms of the voltage, current and power quantities. In the voltage waveforms, the voltage levels were detailed and in the current forms, how to calculate the total output current of the three-phase coupled inductor were shown in detail. In the power waveform, it was shown that the value of the total power was equal to the one proposed. The entire experimental part was developed based on the results found in the simulation, for this reason the experimental results were compared with the simulated ones. There was a small imbalance of currents in the coupled three-phase inductor, but nothing that could detract

from the proper functioning of the prototype. Finally, an analysis of the total harmonic distortion of the voltage was shown. It is observed that in the suggested comparison, the techniques had a similar performance, because in the SVM technique used, it was prioritized to maintain the balance of the currents in the coupled three-phase inductor. Some advantages were verified in using the SVM technique when compared to SPWM, among them the possibility of choosing different vectors and switching sequences, for example aiming to decrease the voltage in a common way, or even change the application time of the vectors in order to increase the performance of the converter. These examples were observed empirically, without corroborating tests.

ACKNOWLEDGMENT

To the Regional University of Blumenau (FURB) and the Santa Catarina State Department of Education – SED, for the financial support, which provided the realization of the project.

REFERENCES

1. Karatsivos, E. D., Adamidis, G. A., & Nathenas, T. G. (2010). A new space vector modulation strategy for multilevel inverters. The XIX International Conference on Electrical Machines - ICEM 2010, 1–7. https://doi.org/10.1109/ICELMACH.2010.5607698

2. Yao, W., Hu, H., & Lu, Z. (2008). Comparisons of space-vector modulation and carrier-based modulation of multilevel inverter. IEEE Transactions on Power Electronics, 23(1), 45–51. https://doi.org/10.1109/TPEL.2007.911865

3. Bueno, E. J., Garcia, R., Marron, M., Urena, J., & Espinosa, F. (2002). Modulation techniques comparison for three levels VSI converters. IEEE 2002 28th Annual Conference of the Industrial Electronics Society. IECON 02, 2, 908–913. https://doi.org/10.1109/IECON.2002.1185393

4. Sourkounis, C., & Al-Diab, A. (2008). A comprehensive analysis and comparison between multilevel space-vector modulation and multilevel carrier-based PWM. 2008 13th International Power Electronics and Motion Control Conference, 1710–1715. https://doi.org/10.1109/EPEPEMC.2008.4635513

5. Hausmann, R., & Barbi, I. (2011). Three-phase DC–AC converter using four-state switching cell. IEEE Transactions on Power Electronics, 26(7), 1857–1867. https://doi.org/10.1109/TPEL.2010.2104335

6. Taschetto, R. L., Cortez, D. F., & Assef, A. A. (2020). Projeto e implementação de um inversor de frequência NPC trifásico com modulação SVPWM controlado por FPGA. Anais do Congresso Brasileiro de Automática 2020, 2(1), 8. https://doi.org/10.48011/asba.v2i1.1468

7. Cortez, D. F. (2012). Inversor trifásico utilizando célula de comutação de múltiplos estados para conexão de um sistema eólico à rede elétrica: Estudo, projeto e implementação [Doctoral dissertation, Universidade Federal de Santa Catarina]. Repositório UFSC. http://repositorio.ufsc.br/xmlui/handle/123456789/99257

8. Pinheiro, H., Botterón, F., Rech, C., Schuch, L., Camargo, R. F., Hey, H. L., Grundling, H. A., & Pinheiro, J. R. (2005). Modulação space vector para inversores alimentados em tensão: Uma abordagem unificada. Sba Controle & Automação Sociedade Brasileira de Automática, 16(1), 13–24. https://doi.org/10.1590/S0103-17592005000100002